Application of machine learning to reflection high-energy electron diffraction images for automated structural phase mapping

Haotong Liang,[1] Valentin Stanev,[1,2,7] Aaron Gilad Kusne,[3,1] Yuto Tsukahara,[4] Kaito Ito,[4] Ryota Takahashi,[4,5] Mikk Lippmaa,[6] and Ichiro Takeuchi[1,2]

[1]*Department of Materials Science and Engineering, University of Maryland, College Park, Maryland 20742, USA*
[2]*Maryland Quantum Materials Center, Department of Physics, University of Maryland, College Park, Maryland 20742, USA*
[3]*National Institute of Standards and Technology, Gaithersburg, Maryland 20899, USA*
[4]*College of Engineering, Department of Electrical and Electronic Engineering, Nihon University, Koriyama 963-8642, Japan*
[5]*JST PRESTO, Saitama 332-0012, Japan*
[6]*Institute for Solid State Physics, University of Tokyo, Kashiwa 277-8581, Japan*
[7]*Data Science and Modeling, Biopharmaceutical Development, AstraZeneca, One MedImmune Way, Gaithersburg, Maryland 20878, USA*

(Received 22 February 2022; accepted 1 June 2022; published 29 June 2022)

We have developed a phase mapping method based on machine learning analysis of reflection high-energy electron diffraction (RHEED) images. RHEED produces diffraction patterns containing a wealth of static and dynamic information and is commonly used to determine the growth rate, the growth mode, and the surface morphology of epitaxial thin films. However, the ability to extract quantitative structural information from the RHEED patterns that appear during film growth is limited by the lack of versatile and automated analysis techniques. We have created a deep learning-based analysis method for automating the identification of different RHEED pattern types that occur during the growth of a material. Our approach combines several supervised and unsupervised machine learning techniques and permits the extraction of quantitative phase composition information. We applied this method to the mapping of the structural phase diagram of Fe_xO_y thin films grown by pulsed laser deposition as a function of growth temperature and oxygen pressure close to the hematite-magnetite phase boundary. The *in situ* RHEED-based mapping method produces results that are qualitatively similar to postsynthesis x-ray diffraction analysis.

DOI: 10.1103/PhysRevMaterials.6.063805

I. INTRODUCTION

The ever-increasing demand for novel functional materials requires innovative approaches to the materials search and discovery process [1]. High-throughput approaches that combine parallelized synthesis with automated characterization have been proposed as a solution to the long-standing problem of long delays in bringing new materials from design or discovery to applications [2]. Such experimental methods have already demonstrated their ability to quickly map the structural phases of a compound as a function of its chemical composition, synthesis parameters, and process conditions—a crucial step in the exploration of new materials [3]. More recently, high-throughput computational methods have augmented such experimental approaches by predicting properties of materials that have not or are difficult to synthesize [4,5]. Besides traditional computational tools, modern machine learning (ML) techniques and *ab initio* techniques are greatly expanding the accessible composition space [6]. Despite the successes of computational techniques, there are many materials systems, even deceptively simple ones such as iron oxides [7–9], for which the formation of metastable polymorphs is extremely sensitive to process conditions. There is thus a definite need and motivation to accelerate experimental phase mapping workflows.

Structural phase mapping has traditionally relied almost exclusively on x-ray diffraction (XRD). The pervasiveness of this technique has led to the development of many specialized computational tools for rapid analysis of the collected data. In some cases, advanced ML methods have been used to automatically generate phase maps from XRD patterns of combinatorial libraries [10–15]. Despite its widespread use, XRD has some significant limitations. In particular, x-ray measurements are challenging for epitaxial thin-film samples because the small volumes of nanoscale films require long exposure times or the use of high-flux synchrotron facilities. Even then, the measurements may prove inconclusive due to the small number of accessible x-ray reflections in epitaxial or highly textured samples. This can contribute to delays in the studies of many promising materials systems.

In this work, we address this rate-limiting constraint of the standard characterization pipeline by developing a method for phase mapping of thin-film samples that relies instead on reflection high-energy electron diffraction (RHEED)—a ubiquitous *in situ* characterization technique commonly used to observe the growth process of nanoscale thin films on single-crystal substrates [16]. RHEED utilizes an electron beam irradiating the surface at grazing incidence, which produces a forward-scattered diffraction pattern of high-intensity streaks and spots on a phosphor screen, providing atomic-level

 ©2022 American Physical Society

structural information. Due to the small penetration depth of electrons in solid matter, RHEED patterns are predominantly sensitive to the topmost atomic layers of an atomically flat surface. For three-dimensional growth, the electron beam can penetrate nanoscale crystallites on a surface and thus also produce a transmission diffraction pattern, which is superimposed on the surface diffraction image.

RHEED is compatible with thin-film deposition systems at gas pressures of up to approximately 100 Pa (or approximately 1 Torr) and has become a standard tool for thin-film growth monitoring. The shape, position, and relative intensity of the observed diffraction features provide a wealth of information on the flatness of the surface, sizes, and orientation of surface unit cells, grains, and domains formation on the surface, growth modes, and the numbers of layers grown. Some of this information, such as the number of unit cell layers that have been grown in layer-by-layer mode, can be easily determined by monitoring the time oscillation of the intensity of the specular reflection or a particular diffraction feature and used as feedback for process control. However, other information on the RHEED pattern is typically analyzed on a qualitative level by visual inspection, and the majority of the quantitative static and dynamic information is discarded. This can be at least partially attributed to the lack of sufficiently general and versatile analysis techniques for the automated processing of RHEED images.

To overcome this limitation, we have developed an ML tool that is specifically designed to automate the classification of RHEED pattern types for the purpose of distinguishing crystalline phases that appear during the film growth (the code and model are publicly available [17]). The tool combines several supervised and unsupervised ML methods and permits the extraction of important information characterizing the crystal structure. The key to identifying regions of interest in diffraction patterns is the use of a deep learning (DL) model that is pretrained on millions of images from ImageNet [18]. DL methods have been behind most of the recent dramatic breakthroughs in computer vision and have been used in many sophisticated algorithms for image analysis tasks. These methods are already being used to analyze materials physics data [19,20]. Yet, so far, DL has not been applied to RHEED images. Our purpose here is to fully embrace the ability of DL to recognize and distinguish complex patterns for novel high-throughput materials development workflows.

II. RELATED WORKS

Only a handful of works have utilized even conventional ML methods in this field. In one notable effort, Vasudevan *et al.* combined principal component analysis (PCA) and *K*-means clustering to analyze sequences of RHEED patterns collected during thin-film growth [21]. A recent work applied this approach during the growth of several perovskite oxide thin-film samples, extracting important dynamic information [22]. The PCA method uses the covariant matrix of vectorized two-dimensional (2D) RHEED patterns to infer the topmost variating directions (principal components) in the patterns. The patterns are projected onto these orthonormal directions to obtain the corresponding weights. This allowed the authors to isolate and visualize distinct growth mode patterns in the form of principal components and their weights. Due to the nature of vectorization, the PCA method is not shift invariant. The RHEED pattern must be aligned by other methods before getting fed into PCA. Besides, the orthonormal constraint on principal components forces them to possess negative intensity values which are not physically meaningful and are hard to interpret. In another work, a convolutional neural network was used to classify surface structures of GaAs films from RHEED patterns taking in two azimuth angles [23]. This work utilized a VGG-like neural network architecture which is not similar to the architecture we proposed here. In their case, classification training labels of each desired surface structure must be provided so that the model can recognize each one of them. The formulation of a classification task here is data inefficient despite being capable of generalizing to other structures. In contrast, our model only extracts generic features and is more interpretable.

III. MATERIALS AND METHODS

As a test of the performance of the ML pipeline, we used it to map the phase diagram of hematite-related structures grown at different temperatures and oxygen pressures. The Fe_xO_y system was selected for the RHEED mapping experiments due to the large variety of known crystal phases that can be stabilized as a function of growth temperature, ambient oxygen pressure, and film thickness [9]. Well-known iron oxides include wüstite (FeO), hematite (α-Fe_2O_3), and magnetite (Fe_3O_4), with multiple known polymorphs for hematite and multiple metastable phases that may be stabilized in thin and possibly epitaxially strained layers [7,8]. All films were grown by pulsed laser deposition on *c*-plane sapphire substrates, which were preannealed in air at 1300 °C for 2 h to obtain a step surface morphology with atomically flat terraces. The films were grown by firing 500 ablation pulses at 2 Hz on a polycrystalline α-Fe_2O_3 target, yielding nominally 40-nm-thick layers. The growth temperature was varied between 400 and 1100 °C at oxygen pressures between 10^{-5} and 10^{-1} Torr (10^{-3}–10 Pa). The 25 kV high-pressure RHEED images were acquired with a 14-bit grayscale digital camera at a rate of two frames per second. The film surfaces were imaged by contact-mode atomic force microscopy (AFM) immediately after deposition. XRD patterns were collected with Cu-$K\alpha_1$ radiation. The signal-to-noise ratio of the XRD scans was limited by the available measurement time, which was set at 1 h per sample. The total synthesis time for each sample, including loading into the vacuum chamber, was less than 30 min.

The crystalline phases present in the thin-film samples were determined by XRD analysis as a baseline to compare with the RHEED analysis. The diffraction peaks were indexed using the reference structures of Fe_xO_y in the Inorganic Crystal Structure Database (ICSD) database to determine the existence of the crystalline phase. The number of accessible diffraction peaks in a symmetric XRD scan of an epitaxial film is limited. Thus, only a handful of *hkl* indexes were used in the analysis of the entire data set. Information on the reference structures and their diffraction peak positions are detailed in Supplemental Material Sec. D [24]. The final XRD phase map is compared with the RHEED phase map in

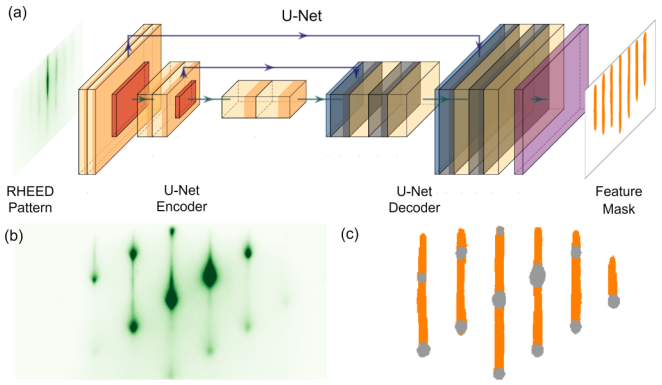

FIG. 1. Schematic diagram of U-Net and example results: (a) A simplified schematic of the U-Net model that takes in an RHEED pattern and outputs a binary mask of features of interest. (b) An example of input RHEED pattern to the U-Net model. Note that this pattern contains both spot and streak features. (c) The predicted masks for spot and streak features are shown in gray and orange colors, respectively.

Sec. V, along with the RHEED phase map to illustrate their similarity.

IV. ML IMAGE ANALYSIS

A. Identification of diffraction features

The diffraction process imprints important structural information in several distinct features of a RHEED image: the location, shape, and intensity of each spot or streak in a diffraction pattern all carry signatures of the structure and morphology of the surface. In terms of image analysis, the intensity variations, which can range from very low to exceeding the dynamic range of the camera, can be particularly problematic. Thus, as the first step in our RHEED image analysis pipeline, we created a system for extracting the diffraction pattern features of interest. This helps to reduce the dynamic range problem since it allows different pattern regions to be separated and analyzed individually.

This step can be approached as a standard image segmentation task. To tackle it, we use U-Net, a convolutional neural network (CNN) architecture shown in Fig. 1(a) that can produce pixel-level masks and has demonstrated state-of-the-art performance in many image segmentation problems [25–27]. U-Net has two components: an encoder and a decoder. The encoder hierarchically extracts relevant image features on different length scales. The decoder merges the output of the encoder with the original image on several different resolution levels and finally outputs a mask with a probability for each pixel to belong to a given class. One additional benefit of the use of U-Net is its intrinsic translational invariance. This allows it to easily handle misaligned patterns caused by camera or sample stage shifts and tilts, in contrast to other algorithms (most notably PCA) that require careful alignment.

The present data set has two distinct classes of patterns related to the surface structure and close to the zero-order Laue zone. Vertical streaks are characteristic of the locally disordered but otherwise flat parts of the film surface, while arrays of spots that do not fall on Laue circles are due to

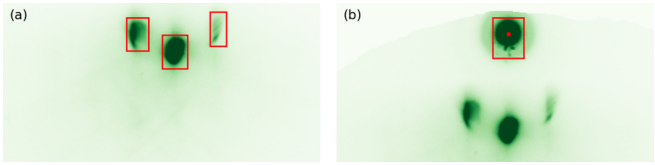

FIG. 2. Different stages of the analysis of RHEED images: (a) Labeled bounding boxes overlaid on an RHEED image. Each rectangular bounding box is drawn around a region labeled by the connected component algorithm. (b) Detected direct beam spot, bound by a box. The red dot shows the center of gravity of the intensity of the beam.

electron transmission through nanoscale crystallites on the surface. Thus, for each RHEED image, two different masks are used to find and separate features with these shapes. Features' binary masks were hand labeled from a set of images using the software DJANGO-LABELLER [28], and were used as labels to train the U-Net model. Each image takes 2–5 min to annotate, depending on the complexity of the RHEED pattern. The time series of RHEED patterns for each film growth experiment was divided into ten sections, and the first image of each section was selected for labeling. In the end, this process yielded 158 labeled RHEED images from 16 recordings representing the growth of 16 distinct thin-film samples. The validation data set was constructed by removing two entire series of RHEED images from the training set, so the model did not train on any images from these two experiments.

The U-Net model was created and trained using the Fastai Python library [18,29]. As the main benchmark of its performance, we use the Dice metric, which evaluates the overlap between the target mask and the predicted mask:

$$\text{Dice} = \frac{2|X \cap Y|}{|X| + |Y|}, \tag{1}$$

where X and Y are the target (true) and predicted binary masks, respectively. This metric is commonly used in image segmentation since it is less susceptible to class-imbalance issues than conventional accuracy.

The Dice metric for the validation set is 0.77, which can be considered high, especially taking into account that the hand-labeling procedure is not perfect. Indeed, by visually inspecting an example prediction and comparing it to the input RHEED pattern, Fig. 1(b), it is clear that the model produces masks with high fidelity [Fig. 1(c)].

B. Separating diffraction regions

Both the shape and the location of each diffraction feature contain important information, thus implementing an accurate method for extracting these properties is crucial. Since the spot and streak features in RHEED images are typically well separated spatially, we use a simple Connected Component labeling algorithm [30,31] implemented by the Scikit-Image Python library [32] to give each connected area a unique label. The algorithm works by finding and connecting neighboring pixels classified by the U-Net as either a spot or a streak. Pixels from disconnected areas are grouped into different regions. Figure 2(a) shows an example of the extracted regions, with their bounding boxes for a diffraction pattern recorded

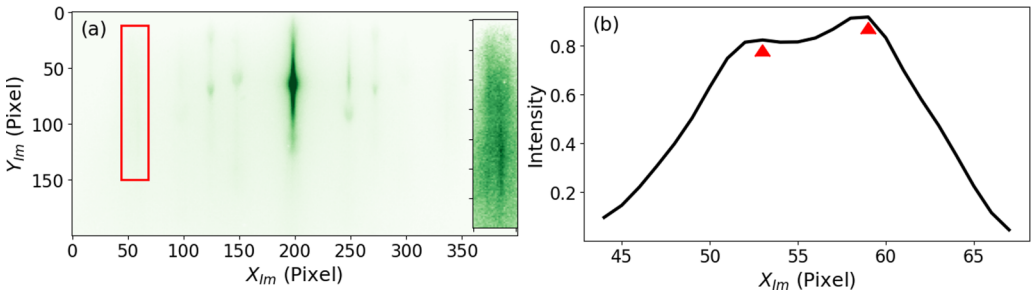

FIG. 3. An illustration of a region covering two features of overlapping diffraction patterns from two phases: (a) The region, bound by a red rectangle, although not visible by eyes at this intensity scale, contains two streak patterns. The zoom-in on the right contains the same box, but with intensity rescaled for better visualization. (b) The integrated one-dimensional intensity variation of the region. The detected peaks are marked with triangles.

on the bare sapphire surface before film growth. Note that the diffraction spots are strongly distorted by substrate chargeup.

C. Tracking the direct beam

When using small substrates in a typical RHEED setup, the finite width of the electron beam means that a part of the direct beam misses the substrate surface and hits the top part of the phosphor screen. The position of the direct beam spot can thus be used as a reference position even when the diffraction pattern is weak or distorted due to surface chargeup. Correctly determining the direct beam spot position is useful for aligning the RHEED images and calibrating the image scale, ensuring that each image is correctly centered. This step ensures that at each time stamp the subsequent algorithm is analyzing the same Laue zone. Algorithmically finding the spot of the direct beam appears trivial since this spot is always located at the top of the RHEED image. However, simply picking the region that is closest to the top part of the image does not work if the sample stage position inside the deposition chamber changes relative to the RHEED screen or the camera position or field-of-view changes—there can be multiple diffraction spots close to the direct beam spot when measurements are done at very low incident beam angles. For this reason, we implemented an object tracking algorithm that matches regions from the current frame to regions from the previous frame. The Intersection over Union (IoU) tracking algorithm is sufficient for this application, as it selects the region that mostly overlaps with the previously matched direct beam region [33]. The degree of overlap is measured by the IoU, which is given by

$$\mathrm{IoU} = \frac{|A \cap B|}{|A \cup B|}, \tag{2}$$

where A and B are the two masked areas of the corresponding regions. Tracking the shared region between image frames is done by finding the region pairs with the highest IoU value. The naïve approach of identifying the direct beam spot as the top one is only used in the first image of the series or when the algorithm loses track of the direct beam, an example of which is shown in Fig. S5 of the Supplemental Material [24]. The center position of the direct beam is computed as the center of gravity of the intensity within the bounding box.

D. Identifying structural phases

A RHEED pattern, as any diffraction pattern, can be viewed as a representation of the collection of real-space periodicities in a sample structure. The horizontal distances between diffraction spots or streaks thus represent different atomic spacings. Even if we ignore any internal structure of the streaks or the vertical positions of the spots, the horizontal spacings alone can be used to generate a fingerprint of a structural phase and thus distinguish different crystal phases. To accelerate computations and get better precision, we only analyze the region around the zero-order Laue circle of the substrate material. This is done by cropping the images and only considering a window below the direct beam, while the size of the window and its distance from the direct beam can be tuned. The trained U-Net model is used to create the spot and streak masks for each cropped image; these masks are then used to extract individual pattern features. For each spot and streak type feature, the signal is integrated vertically, compressing the image data in the analysis window to a one-dimensional feature. The background signal in these one-dimensional features can be easily subtracted after fitting with a simple linear model. The central positions of the diffraction spots and streaks are found by the peak finding algorithm implemented in the SciPy python library [34], which is effective even when a region contains multiple nearly overlapping diffraction features due to connected mask regions as shown in an example in Fig. 3.

The distances between the extracted peak locations and the central specular peak can be used to discover periodicities in the atomic spacings. The analysis of the periodicity is done by finding sets of distances that are multiples of a base distance. This is achieved by determining all horizontal distances present in each image and picking the shortest distance of a peak from the specular position. The algorithm then iteratively extracts the base distances by choosing at each step the smallest unselected distance and adding it to the list of base distances. It then determines all peak distances that are multiples of the current base distance within a given tolerance and marks these distances as selected, assuming that all these peaks belong to the same base distance. The algorithm continues until all distances have been selected, producing a set of base distances characterizing each image.

An illustration of this workflow is shown in Fig. 4(a). The final result of this example is plotted in Fig. 4(b). The

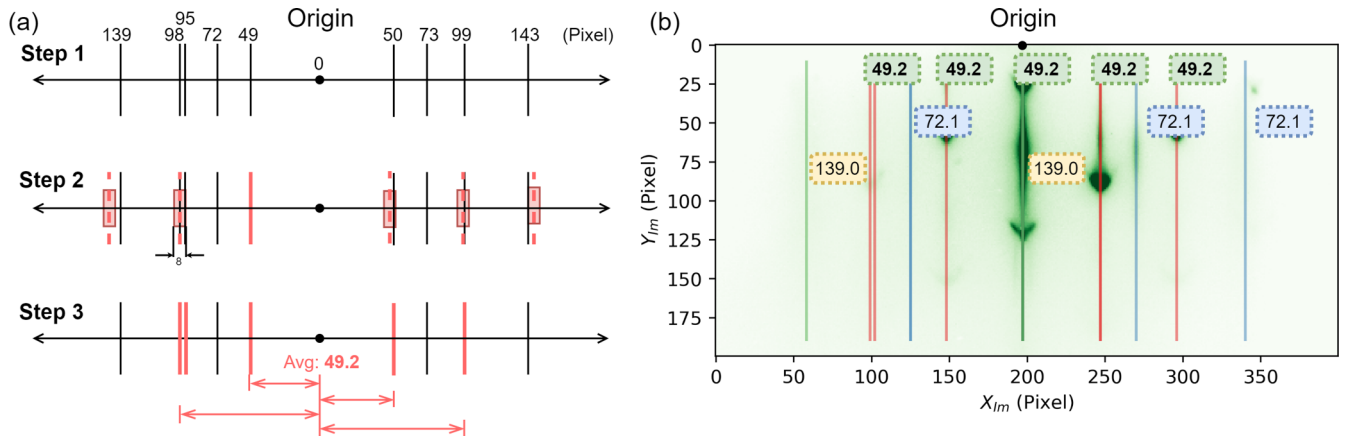

FIG. 4. Analysis of the peak location periodicities: (a) Diagram illustrating how peaks are grouped based on the distance from the origin. Solid lines show peak locations. Step 1: lists all the peaks discovered by our algorithm. Step 2: The peak closest to the origin is selected and labeled in red. Based on this peak, its multiplicity is constructed and shown in the red dash line with an error box. Step 3: Any peaks that are within the range of the error box are considered to be in the same base distance and are labeled in red. (b) All labeled peaks overlaid on the original diffraction pattern. The number shows the average peak distance from the origin normalized by the multiplicity. The red dash line highlights the position of peaks that are analyzed and grounded in (a).

detailed algorithm is described in Supplemental Material Sec. A [24].

The spacing in pixel space is further converted into the reciprocal space using the relationship

$$ng_h = \frac{n\alpha l}{L} k_0 \tag{3}$$

where n is the periodicity, l is the feature length in pixels, α is the physical size of a pixel, L is the camera length, and k_0 is the momentum of incident electron beam. This converted distance could be directly used to match with reciprocal lattice vectors of the reference structures, which helps to rule out the phases on the surface. Starting from a raw RHEED image, it takes less than 0.1 sec to run the entire analysis pipeline to obtain the summarized periodicity and intensity data for the main peaks making real-time processing feasible.

V. PHASE MAPPING BY REGION INTENSITY

The horizontal spacing information is sufficient for detecting the presence of a given phase but not for quantifying its abundance. We developed an algorithm (described in Supplemental Material Sec. B [24]) to compute the relative intensity for each base peak distance, helping to quantify the phase composition of a multiphase sample. The algorithm computes the intensity relative to the total intensity for each identified base distance for each RHEED image. However, different RHEED images have different base distances; thus, a "unification" step is required to express them as a fixed-length vector for later pattern clustering. Here, the density-based spatial clustering of applications with noise (DBSCAN) algorithm [35] is used to group similar base distances into clusters. The number of clusters, i.e., the overall number of distinct base distances, determines the total number of base distances, thus the size of the vector. Each vector provides a unique representation of the RHEED image of a sample, with components representing the relative intensity at a specific base distance, as shown in Fig. 5. A human expert or machine could look for phases that are continuous in parameter spaces to confirm the analysis. Note the conceptual similarity of the process with the phase mapping algorithms based on XRD data [10–15]. Figure 5(b) shows a growth parameter phase map with extracted feature vectors for the iron oxide growth mapping experiment which we can compare to a human-labeled XRD mapping result in Fig. 5(c). Here, the sample synthesis in condition (10^{-A} Torr, B °C) is denoted as A–B (e.g., 10^{-5} Torr, 300 °C is labeled as 5–300). This notation is applied to the rest of the paper for ease of understanding. As can be seen there, regions containing similar vectors generally match well with the XRD measurement shown in Fig. 5(c). One notable deviation is the clear difference between the two highest-temperature samples, grouped based on XRD data. These samples show quite distinct RHEED patterns.

VI. INTERPRETATION AND ANALYSIS OF RHEED FEATURE MAPPING

We first present an analysis of just the RHEED features to show that one can achieve a semiquantitative analysis of phase mapping using RHEED data only. Phase compositions can be inferred from the extracted phase map from RHEED patterns when combined with knowledge of known materials phases and their structures. The phase map predominately consists of two distances: 13.83 and 20.38 nm^{-1}. α-Fe_2O_3 is isostructural to sapphire thus epitaxial growth is expected. The first distance, 13.83 nm^{-1}, is in proximity to the α-Fe_2O_3 $(10\bar{1}0)$ plane, which is perpendicular to the (0001) substrate plane with the beam incident in the $[11\bar{2}0]$ direction. Thus, the first distance shown as a green pie slice in the phase map represents the epitaxially grown hematite (α-Fe_2O_3) phase. The second distance, 20.38 nm^{-1}, appears at both low and high temperatures and suggests a different phase. Comparing the distance with various lattice planes of high-symmetry Fe_xO_y phases, we identify the distance to be the Fe_3O_4 $(02\bar{2})$ plane which is perpendicular to the (111) plane. There are three samples (2-524, 2-805, and 3-1048) that cannot be fully explained by

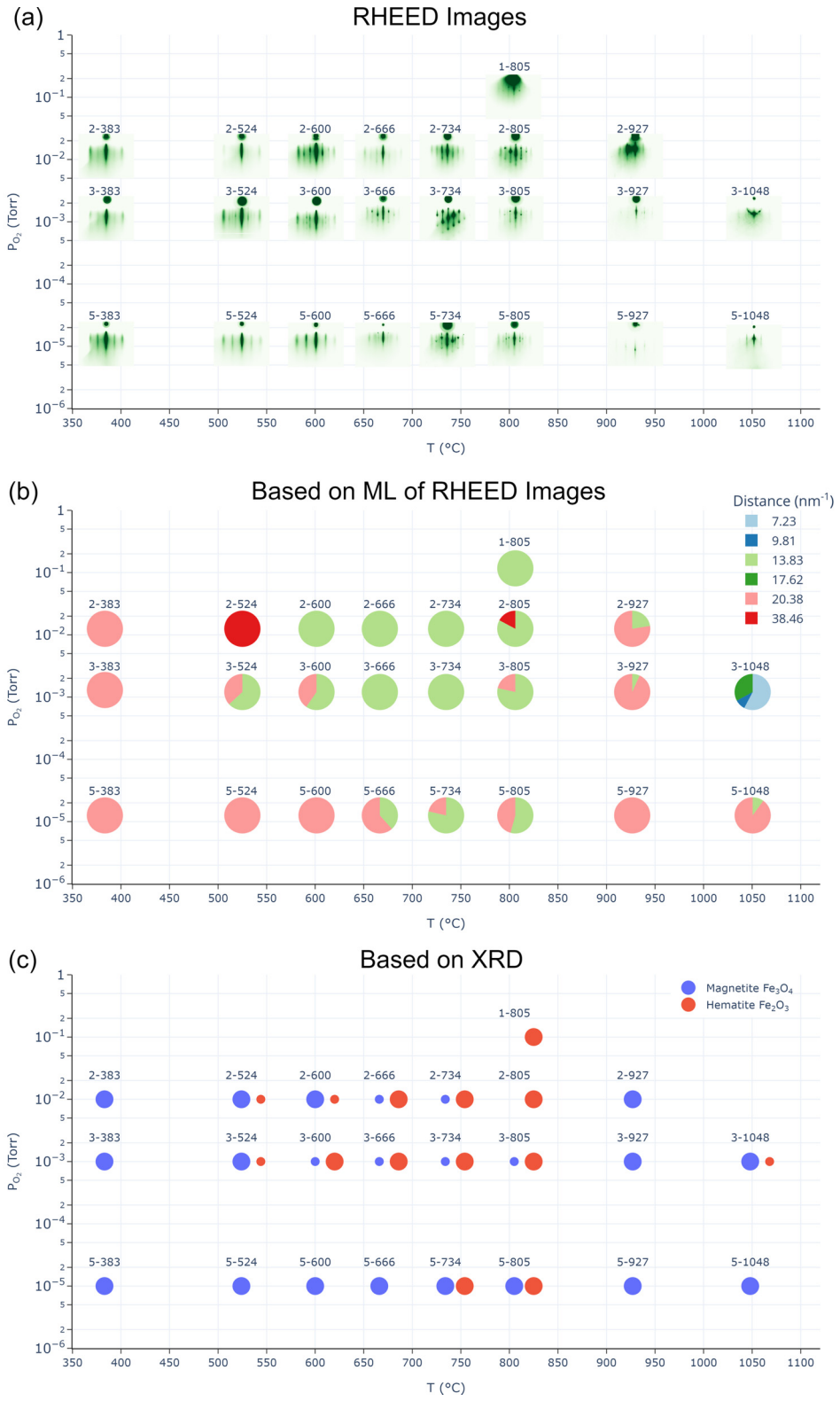

FIG. 5. Phase mapping of iron oxide films: (a) Raw RHEED images recorded at the end of each deposition. (b) The extracted regions' intensities of each base distance from the RHEED pattern form a feature vector. Each feature vector is represented by a pie chart where each pie slice's area shows the relative intensity of each base distance. The color encodes the base distance of the region intensity as shown in the legend. The unit of the distance is nm^{-1}. (c) The red and blue scatter points show the XRD phase map of the hematite (α-Fe_2O_3) and magnetite (Fe_3O_4) phases, respectively. The presence of a phase is plotted as a circle. The size of the circle indicates if the phase is major or trace material in a particular sample. Sample identifier notation: sample made at 10^{-A} Torr at B °C is denoted as A-B. For instance, the sample 5-600 was made at 10^{-5} Torr of P_{O2} at the substrate temperature of 600 °C.

these two distances. The 38.46-nm^{-1} spacing, which appears in 2-524 and 2-805, is close to the third-order diffraction pattern of the α-Fe_2O_3 $(10\bar{1}0)$ and the second-order diffraction pattern of the Fe_3O_4 $(02\bar{2})$. The absolute intensity for samples in the low-temperature region (350–600 °C), including 2-524, is quite low, suggesting low crystallinity of Fe_3O_4 and α-Fe_2O_3 due to kinetically limited growth. Similar reasoning can also be applied to sample 2-805, where the appearance of 38.46 nm^{-1} indicates that a trace amount of Fe_3O_4 coexists with α-Fe_2O_3. The last sample, 3-1048, shows signs of surface reconstruction where the two major distances, 7.23 and 9.81 nm^{-1}, are approximately equal to one-half of the α-Fe_2O_3 $(10\bar{1}0)$ and Fe_3O_4 $(02\bar{2})$ planes, respectively. The last distance, 17.62 nm^{-1}, unexpectedly matches the Fe_3O_4 $(1\bar{2}1)$ plane suggesting that the Fe_3O_4 layer is in-plane rotated by 30 ° from the original direction. The appearance of 13.83 nm^{-1} in sample 5-1048 might be due to the substrate and not the α-Fe_2O_3 phase because of the 3D island growth of Fe_3O_4 that leaves some part of the substrate surface exposed.

Combinations of extracted features from RHEED with XRD patterns and AFM images provide more in-depth information regarding the phase distribution. The analysis of XRD patterns is detailed in Supplemental Material Sec. D [24]. The majority of XRD phase mapping for α-Fe_2O_3 and Fe_3O_4 matches the mapping from RHEED (Fig. 5). There are some samples where only a trace amount of material is present, and they are only discernible in the XRD patterns. The absence of certain phases in RHEED of these samples could suggest the trace phase is covered under the surface. For growth experiments performed at high ambient pressures in the 100-mTorr range, weaker diffraction features may become invisible due to the lower signal-to-noise ratio when strong electron scattering from the ambient gas increases the background intensity. From AFM images, the Fe_3O_4 phase formed truncated triangular prism nanostructures in the high-temperature region (>900 °C) but transformed into a flat surface in the low-temperature region. Due to the kinetic limitation of Fe_3O_4 film growth in the low-temperature regime, these films have relatively low crystallinity, which leads to low feature intensities in both XRD and RHEED measurements. The RHEED data suggest that there is an α-Fe_2O_3 layer on the surfaces of samples 2-927, 3-927, and 5-1048, but the thickness is only a few unit cells, which makes it hard to detect by XRD. The thickness of the α-Fe_2O_3 component around those 3D Fe_3O_4 structures is at most 2–3 nm, as measured by AFM.

The thin-film phase diagram of iron oxides obtained in this work shows agreement with the calculated bulk phase diagram [36] at high temperatures while deviating at low temperatures. The gradual transition in phase composition around 800 °C shows that the Fe_3O_4 phase is stabilized at high temperature and low oxygen partial pressure regions. The formation of the α-Fe_2O_3 and Fe_3O_4 mixture could possibly be due to the nonequilibrium nature of the thin-film deposition process. The realization of Fe_3O_4 on Al_2O_3 (0001) in films grown by PLD from an α-Fe_2O_3 target has been reported previously when the substrate temperature was 450 °C at an oxygen partial pressure of 10^{-6} Torr [37]. One possible explanation is the high-energy plasma of the PLD process enables the formation of Fe_3O_4 at the surface, and subsequent surface-to-bulk diffusion is limited by the low substrate temperature [38]. Generally, there can be a deviation in thin-film phase formation from bulk phases due to the competition between growth and oxidation: the reaction rate of oxidation can be slower than the growth rate at low temperature [39], thereby leading to the formation of the lower oxygen-content phase. The region of Fe_3O_4 identified here is comparable with the result from Tiwari *et al.* [37]. The lattice parameter of the Fe_3O_4 is larger than the bulk value in their study due to the 8% lattice mismatch between Fe_3O_4 (111) and Al_2O_3 (0001). However, our XRD patterns show the lattice parameter of Fe_3O_4 or the inverse spinel structure shrinks as the oxygen pressure increases. This may be due to Fe^{2+} ions in octahedral sites being oxidized and transferred to the nearby tetrahedral sites, thus creating vacancies in the material [40]. Thus, in the region (600–800 °C) with higher temperatures, $Fe_{3-\delta}O_4$ or even γ-Fe_2O_3 transforms into the thermodynamically stable α-Fe_2O_3.

Similarly, at elevated temperatures, the reverse transition can happen. In sample 3-1048, the two distances (7.23 and 9.81 nm^{-1}) are most likely due to surface reconstruction of α-Fe_2O_3 and Fe_3O_4. Although single-phase Fe_3O_4 (111) does not reconstruct [41], there is a well-known "biphase" surface structure on oxidized or mineral α-Fe_2O_3 (0001) surfaces [42–44]. Based on the sample's experimental condition and the bulk phase diagram, it is unlikely for α-Fe_2O_3 and FeO domains to coexist on the surface. However, the structure model where a thin layer of Fe_3O_4 overlays on top of the α-Fe_2O_3 proposed by Lanier *et al.* agrees with our XRD measurement [43]. The semicoherent hexagon-on-hexagon interface structure forms a hexagonal Moiré lattice ($a = 4.36$ nm) with a 30 ° in-plane rotation from the α-Fe_2O_3 (0001) direction. The (11) diffraction of the Moiré lattice has a similar magnitude ($g_{(11)} = 2.88\ nm^{-1}$) as the spacing (2.60 nm^{-1}) between each small streak from the reconstruction pattern.

VII. FUTURE PERSPECTIVE

The use of an automated pattern feature and phase extraction pipeline opens the possibility of applying active learning techniques for fully autonomous process control [45–49]. This can be utilized for mapping growth parameters or optimizing growth conditions of a particular phase without human intervention or manual evaluation of RHEED patterns. Since the pipeline operation is faster than the film growth experiment, it is possible to fully utilize deposition instrument time, which cannot be achieved if XRD (carried out post deposition) is used as the source of process feedback information. We expect the application of ML methods to electron diffraction patterns to significantly speed up the development of new thin-film materials where metastable phases or structural phase boundaries occur in the accessible process parameter space. Clearly, temperature and gas pressure are not the only parameters that can be varied. Equally accessible for the PLD process would be, for example, deposition laser fluence, ablation area, growth rate, and, of course, composition. While such mappings are difficult to visualize and analyze by a human operator due to the multidimensional nature of the parameter space, active learning methods do not suffer from the same handicap. We thus expect the combination of the RHEED image analysis

pipeline described here with active learning process control to revolutionize thin-film materials development.

VIII. CONCLUSIONS

We have developed an ML pipeline for automatically distinguishing different structural phases in thin films from RHEED images. We have applied the ML analysis to RHEED images taken during the growth of a series of Fe_xO_y thin films deposited by PLD over broad ranges of deposition temperatures and oxygen pressures in order to obtain a process-phase diagram. Microstructural data on materials phases present in the thin-film samples were also characterized by XRD and AFM. The pipeline produced a phase diagram with distinct regions which are in good agreement with a phase map obtained from XRD, validating the use of RHEED data for automatically generating a structural phase map. The method based on general features extracted from RHEED is thus sufficiently versatile for analyzing the growth of any material and is not specific to the iron oxides used in this demonstration and it could run in parallel with the film deposition process. In the future, the pipeline could be deployed onto optimizing film surface structure or hunting for new metastable phases by exploring the full PLD parameters space.

ACKNOWLEDGMENTS

This work was supported by ONR MURI N00014172661 and NIST Cooperative Agreement No. 70NANB17H301. The work at the University of Tokyo was supported by the JST-Mirai Program "Materials Exploration Platform; Expanding Search Space by high-throughput technology," Grant No. JPMJMI21G2, by ATLA Innovative Science and Technology Initiative for Security (Grant No. JPJ004596), JSPS KAKENHI (Grant No. 20H02622), and the Gordon and Betty Moore Foundations EPIQS Initiative through ICAM-I2CAM, Grant GBMF5305.

[1] K. Alberi, M. B. Nardelli, A. Zakutayev, L. Mitas, S. Curtarolo, A. Jain, M. Fornari, N. Marzari, I. Takeuchi, M. L. Green, M. Kanatzidis, M. F. Toney, S. Butenko, B. Meredig, S. Lany, U. Kattner, A. Davydov, E. S. Toberer, V. Stevanovic, A. Walsh *et al.*, The 2019 materials by design roadmap, J. Phys. D: Appl. Phys. **52**, 013001 (2018).

[2] H. Koinuma and I. Takeuchi, Combinatorial solid-state chemistry of inorganic materials, Nat. Mater. **3**, 429 (2004).

[3] A. Ludwig, Discovery of new materials using combinatorial synthesis and high-throughput characterization of thin-film materials libraries combined with computational methods, npj Comput. Mater. **5**, 70 (2019).

[4] W. Sun, C. J. Bartel, E. Arca, S. R. Bauers, B. Matthews, B. Orvañanos, B. R. Chen, M. F. Toney, L. T. Schelhas, W. Tumas, J. Tate, A. Zakutayev, S. Lany, A. M. Holder, and G. Ceder, a map of the inorganic ternary metal nitrides, Nat. Mater. **18**, 732 (2019).

[5] M. R. Filip and F. Giustino, The geometric blueprint of perovskites, Proc. Natl. Acad. Sci. USA. **115**, 5397 (2018).

[6] K. T. Butler, D. W. Davies, H. Cartwright, O. Isayev, and A. Walsh, Machine learning for molecular and materials science, Nature (London) **559**, 547 (2018).

[7] S. Lee and H. Xu, Size-Dependent phase map and phase transformation kinetics for nanometric Iron(III) oxides ($\gamma \rightarrow \epsilon \rightarrow \alpha$ Pathway), J. Phys. Chem. C **120**, 13316 (2016).

[8] L. MacHala, J. Tuček, and R. Zbořil, Polymorphous transformations of nanometric Iron(III) Oxide: a review, Chem. Mater. **23**, 3255 (2011).

[9] S. M. Suturin, A. M. Korovin, S. V. Gastev, M. P. Volkov, A. A. Sitnikova, D. A. Kirilenko, M. Tabuchi, and N. S. Sokolov, Tunable polymorphism of epitaxial iron oxides in the Four-in-One Ferroic-on-GaN system with magnetically ordered α-, γ-, ϵ-Fe_2O_3, and Fe_3O_4 layers, Phys. Rev. Materials **2**, 073403 (2018).

[10] C. J. Long, J. Hattrick-Simpers, M. Murakami, R. C. Srivastava, I. Takeuchi, V. L. Karen, and X. Li, Rapid structural mapping of ternary metallic alloy systems using the combinatorial approach and cluster analysis, Rev. Sci. Instrum. **78**, 072217 (2007).

[11] C. J. Long, D. Bunker, X. Li, V. L. Karen, and I. Takeuchi, Rapid identification of structural phases in combinatorial thin-film libraries using x-Ray diffraction and non-negative matrix factorization, Rev. Sci. Instrum. **80**, 103902 (2009).

[12] R. LeBras, T. Damoulas, J. M. Gregoire, A. Sabharwal, C. P. Gomes, and R. B. van Dover, *Constraint Reasoning and Kernel Clustering for Pattern Decomposition with Scaling BT - Principles and Practice of Constraint Programming CP 2011*, edited by J. Lee (Springer Berlin Heidelberg, Berlin, Heidelberg, 2011), pp. 508–522.

[13] A. G. Kusne, T. Gao, A. Mehta, L. Ke, M. C. Nguyen, K. M. Ho, V. Antropov, C. Z. Wang, M. J. Kramer, C. Long, and I. Takeuchi, On-the-Fly machine-learning for high-throughput Experiments: search for rare-earth-free permanent magnets, Sci. Rep. **4**, 6367 (2014).

[14] S. K. Suram, Y. Xue, J. Bai, R. Le Bras, B. Rappazzo, R. Bernstein, J. Bjorck, L. Zhou, R. B. Van Dover, C. P. Gomes, and J. M. Gregoire, Automated phase mapping with AgileFD and its application to light absorber discovery in the v-mn-nb oxide system, ACS Comb. Sci. **19**, 37 (2017).

[15] V. Stanev, V. V. Vesselinov, A. G. Kusne, G. Antoszewski, I. Takeuchi, and B. S. Alexandrov, Unsupervised phase mapping of x-ray diffraction data by nonnegative matrix factorization integrated with custom clustering, npj Comput. Mater. **4**, 43 (2018).

[16] S. Hasegawa, *Reflection High-Energy Electron Diffraction, Characterization Of Materials*, 2nd ed. (Wiley-Interscience, Hoboken, 2003), p. 1925.

[17] https://github.com/AuroraLHT/rhana.

[18] J. Howard and S. Gugger, Fastai: a layered API for deep learning, Inf., **11**, 108 (2020).

[19] Y. Zhang, A. Mesaros, K. Fujita, S. D. Edkins, M. H. Hamidian, K. Ch'ng, H. Eisaki, S. Uchida, J. C. S. Davis, E. Khatami, and E. A. Kim, Machine learning in electronic-quantum-matter imaging experiments, Nature (London) **570**, 484 (2019).

[20] M. Ziatdinov, O. Dyck, A. Maksov, X. Li, X. Sang, K. Xiao, R. R. Unocic, R. Vasudevan, S. Jesse, and S. V. Kalinin, Deep learning of atomically resolved scanning transmission electron

microscopy Images: chemical identification and tracking local transformations, ACS Nano **11**, 12742 (2017).

[21] R. K. Vasudevan, A. Tselev, A. P. Baddorf, and S. V. Kalinin, Big-Data reflection high energy electron diffraction analysis for understanding epitaxial film growth processes, ACS Nano **8**, 10899 (2014).

[22] S. R. Provence, S. Thapa, R. Paudel, T. K. Truttmann, A. Prakash, B. Jalan, and R. B. Comes, Machine learning analysis of perovskite oxides grown by molecular beam epitaxy, Phys. Rev. Materials **4**, 083807 (2020).

[23] J. Kwoen and Y. Arakawa, Classification of reflection high-energy electron diffraction pattern using machine learning, Cryst. Growth Des. **20**, 5289 (2020).

[24] See Supplemental Material at http://link.aps.org/supplemental/10.1103/PhysRevMaterials.6.063805 for more detailed information regarding the RHEED analysis algorithm, U-Net architecture, XRD and AFM analyses, and drifting of the direct beam.

[25] O. Ronneberger, P. Fischer, and T. Brox, *U-Net: Convolutional Networks for Biomedical Image Segmentation BT - Medical Image Computing and Computer-Assisted Intervention MICCAI 2015*, edited by N. Navab, J. Hornegger, W. M. Wells, and A. F. Frangi (Springer International Publishing, Cham, 2015), pp. 234–241.

[26] K. He, X. Zhang, S. Ren, and J. Sun, Deep residual learning for image recognition, in *2016 IEEE Conference on Computer Vision and Pattern Recognition (CVPR)* (IEEE, 2016), pp. 770–778.

[27] L. Liu, J. Cheng, Q. Quan, F. X. Wu, Y. P. Wang, and J. Wang, A survey on u-shaped networks in medical image segmentations, Neurocomputing **409**, 244 (2020).

[28] G. French, *Django-Labeller*, https://github.com/Britefury/django-labeller.

[29] Y. Sugawara, S. Shiota, and H. Kiya, Super-resolution using convolutional neural networks without any checkerboard artifacts, in *Proceedings - International Conference on Image Processing, ICIP* (IEEE Computer Society, 2018), pp. 66–70.

[30] C. Fiorio and J. Gustedt, Two linear time union-find strategies for image processing, Theor. Comput. Sci. **154**, 165 (1996).

[31] K. Wu, E. Otoo, and K. Suzuki, Optimizing two-pass connected-component labeling algorithms, Pattern Anal. Appl. **12**, 117 (2009).

[32] S. der Walt, J. L. Schönberger, J. Nunez-Iglesias, F. Boulogne, J. D. Warner, N. Yager, E. Gouillart, and T. Yu, Scikit-Image: image processing in Python, PeerJ **2**, e453 (2014).

[33] E. Bochinski, V. Eiselein, and T. Sikora, High-speed tracking-by-detection without using image information, in *2017 14th IEEE International Conference on Advanced Video and Signal Based Surveillance, AVSS 2017* (Institute of Electrical and Electronics Engineers Inc., 2017), pp. 1–6.

[34] P. Virtanen, R. Gommers, T. E. Oliphant, M. Haberland, T. Reddy, D. Cournapeau, E. Burovski, P. Peterson, W. Weckesser, J. Bright, S. J. van der Walt, M. Brett, J. Wilson, K. J. Millman, N. Mayorov, A. R. J. Nelson, E. Jones, R. Kern, E. Larson, C. J. Carey *et al.*, SciPy 1.0: fundamental algorithms for scientific computing in python, Nat. Methods **17**, 261 (2020).

[35] M. Ester, H.-P. Kriegel, J. Sander, and X. Xu, A density-based algorithm for discovering clusters in large spatial databases with noise, in *Proceedings of the Second International Conference on Knowledge Discovery and Data Mining* (AAAI Press, Portland, Oregon, 1996), pp. 226–231.

[36] G. Ketteler, W. Weiss, W. Ranke, and R. Schlögl, Bulk and surface phases of iron oxides in an oxygen and water atmosphere at low pressure, Phys. Chem. Chem. Phys. **3**, 1114 (2001).

[37] S. Tiwari, R. Prakash, R. J. Choudhary, and D. M. Phase, Oriented growth of Fe_3O_4 thin film on crystalline and amorphous substrates by pulsed laser deposition, J. Phys. D: Appl. Phys. **40**, 4943 (2007).

[38] P. P. Balakrishnan, M. J. Veit, U. S. Alaan, M. T. Gray, and Y. Suzuki, Metallicity in $SrTiO_3$ substrates induced by pulsed laser deposition, APL Mater. **7**, 11102 (2019).

[39] X. D. Zhu, W. Si, X. X. Xi, and Q. Jiang, Oxidation kinetics in SrTiO3 homoepitaxy on $SrTiO_3$(001), Appl. Phys. Lett. **78**, 460 (2001).

[40] F. Schedin, E. W. Hill, G. Van Der Laan, and G. Thornton, Magnetic properties of stoichiometric and nonstoichiometric ultrathin Fe_3O_4(111) films on Al_2O_3(0001), J. Appl. Phys. **96**, 1165 (2004).

[41] M. Ritter and W. Weiss, Fe_3O_4(111) surface structure determined by LEED crystallography, Surf. Sci. **432**, 81 (1999).

[42] S. Liu, S. Wang, J. Guo, and Q. Guo, Polarity and surface structural evolution of iron oxide films, RSC Adv. **2**, 9938 (2012).

[43] C. H. Lanier, A. N. Chiaramonti, L. D. Marks, and K. R. Poeppelmeier, The Fe_3O_4 origin of the "Biphase" reconstruction on α-Fe_2O_3(0 0 0 1), Surf. Sci. **603**, 2574 (2009).

[44] A. Kiejna and T. Pabisiak, Mixed termination of hematite (α-Fe_2O_3)(0001) surface, J. Phys. Chem. C **117**, 24339 (2013).

[45] L. M. Roch, F. Häse, C. Kreisbeck, T. Tamayo-Mendoza, L. P. E. Yunker, J. E. Hein, and A. Aspuru-Guzik, ChemOS: an orchestration software to democratize autonomous discovery, PLoS One **15**, e0229862 (2020).

[46] P. Nikolaev, D. Hooper, F. Webber, R. Rao, K. Decker, M. Krein, J. Poleski, R. Barto, and B. Maruyama, Autonomy in materials Research: a case study in carbon nanotube growth, npj Comput. Mater. **2**, 1 (2016).

[47] A. G. Kusne, H. Yu, C. Wu, H. Zhang, J. Hattrick-Simpers, B. DeCost, S. Sarker, C. Oses, C. Toher, S. Curtarolo, A. V. Davydov, R. Agarwal, L. A. Bendersky, M. Li, A. Mehta, and I. Takeuchi, On-the-Fly closed-loop materials discovery via bayesian active learning, Nat. Commun. **11**, 1 (2020).

[48] A. E. Gongora, B. Xu, W. Perry, C. Okoye, P. Riley, K. G. Reyes, E. F. Morgan, and K. A. Brown, a bayesian experimental autonomous researcher for mechanical design, Sci. Adv. **6**, eaaz1708 (2020).

[49] I. Ohkubo, Z. Hou, J. N. Lee, T. Aizawa, M. Lippmaa, T. Chikyow, K. Tsuda, and T. Mori, Realization of closed-loop optimization of epitaxial titanium nitride thin-film growth via machine learning, Mater. Today Phys. **16**, 100296 (2021).